

Sand Ripple Characterization Using an Extended Synthetic Aperture Sonar Model and Parallel Sampling Method

Chao Chen, *Student Member, IEEE*, Alina Zare, *Senior Member, IEEE*, and J. Tory Cobb, *Member, IEEE*

Abstract—The aim of this work is to characterize the seafloor by estimating invariant sand ripple parameters from synthetic aperture sonar (SAS) imagery. Using a hierarchical Bayesian framework and a known sensing geometry, a method for estimating sand ripple frequency, amplitude, and orientation values from a single SAS image, as well as from sets of SAS imagery over an area, is presented. This is accomplished through the development of an extended model for sand ripple characterization and a Metropolis-within-Gibbs sampler to estimate sand ripple frequency, amplitude, and orientation characteristics for multispect high-frequency side-look sonar data. Results are presented on synthetic and measured SAS imagery that indicate the ability of the proposed method to estimate desired sand ripple characteristics.

Index Terms—Markov chain Monte Carlo (MCMC) sampling, Metropolis-within-Gibbs, sand ripple, seafloor mapping, synthetic aperture sonar (SAS).

I. INTRODUCTION

HIGH-RESOLUTION imaging sonars, such as side-look synthetic aperture sonar (SAS), can produce near-photographic-quality images of the seafloor. In these images, natural textures such as sand ripples formed by current-sediment interaction are easily identifiable to the human eye. In this paper, we seek to estimate the invariant salient features of these sand ripple beds using a model that encompasses the sensing geometry of a side-look SAS system and the backscattered return from the rippled seafloor. The model yields parameters, namely, ripple frequency, amplitude, and orientation, that are invariant to sensor range and altitude. By estimating parameters that are invariant to sensing geometry, the approach provides a framework to leverage knowledge gained from multiple views or passes over the same region with varying sensing geometry.

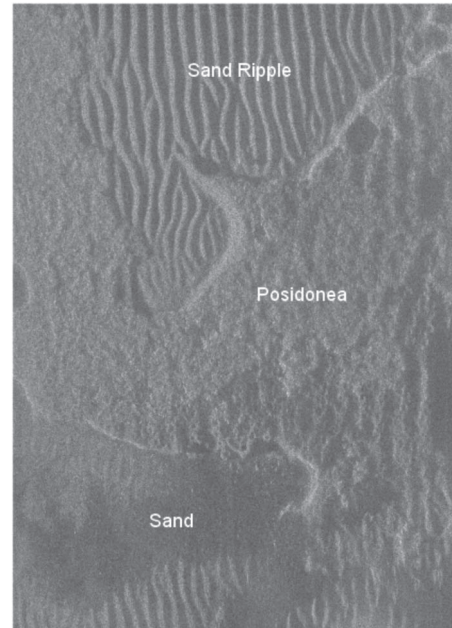


Fig. 1. SAS image containing sand ripples, posidonea (a type of sea grass), and hard-packed sand.

A. SAS System

SAS systems differ from conventional side-scan sonar where, instead of each ping echo return being processed independently, SAS systems coherently combine data from multiple sonar pings along a known track. This allows for the ability to produce high-resolution images at low frequencies and over a large range [1]–[3]. SAS imagery can have resolutions down to the centimeter scale and range values up to hundreds of meters [3].

SAS imagery can be considered as an intensity representation of the backscattered acoustic energy [1]. Fig. 1 shows examples of different seafloor types present in SAS imagery. Since the scattering process is related to the seafloor type, the backscattered acoustic wave reflects the characteristics of different seafloor types, allowing the sonar imagery to be used to distinguish between these seafloor types. SAS imagery is used in this paper due to its high spatial resolution, allowing for the information needed to conduct sand ripple characterization to be collected. In our future work, the feasibility of applying the proposed method to imagery from other sonar systems, e.g., conventional side-scan sonar, or sector scan sonar, can be investigated.

Manuscript received November 3, 2014; revised January 12, 2015 and February 13, 2015; accepted April 15, 2015. This work was supported by the Office of Naval Research, Code 321, under Grant N00014-14-1-0368.

C. Chen and A. Zare are with the Department of Electrical and Computer Engineering, University of Missouri, Columbia, MO 65211 USA (e-mail: ccwwf@mail.missouri.edu; zarea@missouri.edu).

J. T. Cobb is with the Naval Surface Warfare Center, Panama City, FL 32407 USA (e-mail: james.cobb@navy.mil).

Color versions of one or more of the figures in this paper are available online at <http://ieeexplore.ieee.org>.

Digital Object Identifier 10.1109/TGRS.2015.2424837

B. Related Work on Sand Ripple Characterization

Ripple frequency, amplitude, and orientation have been estimated to characterize sand ripples previously in the literature. Previous methods for sand ripple characterization generally fall into two categories: manual analysis and frequency analysis. In studies that rely on manual analysis [4], [5], significant individual observational bias may occur, and results may not be reliably repeatable. Particularly when dealing with a large number of images, manual analysis is neither an efficient nor practical processing option. To overcome these limitations, approaches based on frequency transformations such as Fourier [6] and Radon [7] transforms have been developed. These methods generally extract ripple frequency and orientation by transforming the ripple image data into the frequency domain and examining the relative positions of the power spectral peaks. As ripple amplitude estimation methods generally require the use of specialized methods and equipment, ripple amplitude is more difficult to measure than ripple frequency and is often omitted [8].

Previous studies on sand ripple characterization also included methods for predicting ripple geometry given known wave parameters and grain size. Substantial laboratory [9], [10] and field studies [11], [12] have been conducted for a large range of these parameters. These studies were generally based on either laboratory or field data, but rarely both. Wiberg and Harris [8] conducted one of the few studies using both laboratory and field data. They estimated ripple amplitude, wavelength, and steepness parameters using approaches that relied on the determination of the ripple type among a number of categories. Their approach was evaluated by comparing estimated and measured ripple parameters. Ripple parameters were measured *in situ* using stereo photography and electrical conductivity [13]–[16]. However, these measurements can only be carried out over very small regions (e.g., 1–5 m in length). Acoustic backscatter instruments have allowed for the collection of large swaths of imagery displaying the seafloor morphology. Different kinds of acoustic backscatter instruments have been utilized in sand ripple studies. Hanes *et al.* [17] investigated the properties of wave-formed sand ripples at Duck, North Carolina, using an acoustic multiple transducer array and tested the Nielsen [18] model and the Wiberg and Harris [8] model on these ripples.

With the wide use of acoustic backscatter instruments, autonomous algorithms for analyzing sand ripples using backscattered signals (images) became a key issue of interest. Skarke and Trembanis [19] analyzed side-scan sonar images using fingerprint analysis techniques that could evaluate a previously unused parameter, the spatial density of ripple defects. Cobb and Principe [20], [21] characterized seabed texture (including sand ripples) in SAS images using a parametric model based on the autocorrelation function of the intensity image. Williams and Coiras [22] established a model for sand ripple detection in SAS imagery by searching for patterns characterized by the highlight–shadow pairs. Based on the data collected by the backscattering system in [23], Tang *et al.* [24] demonstrated the potential of estimating ripple wavelength and amplitude from backscattering images and proposed a preliminary estimation method by relating the scattering strength to the local slope of the ripple surface. In many of these previous studies,

however, any estimation of ripple amplitude relied on accurate and calibrated scattering strength. In the proposed approach, ripple frequency, amplitude, and orientation are estimated using shadow and occlusion information in the imagery such that these parameters can be estimated using uncalibrated (in terms of scattering strength) imagery.

Accurate estimates of the sand ripple frequency, amplitude, and orientation characteristics can be ultimately used within a number of applications of SAS imagery, including detection and classification of targets in a scene [25], [26], seabed segmentation and classification [20], [21], and others.

This paper extends our previous work [27] on sand ripple characterization in four aspects: estimation of ripple orientation, investigation of additional seafloor scattering models, introduction of a parallel sampling method, and extended experimentation to test the approach. Considering that sand ripple crests are rarely parallel to sonar tracks, this paper presents an approach that adds a new parameter to estimate the ripple orientation, in addition to the ripple frequency and amplitude parameters. The proposed approach also extends the previously used Gaussian scattering model by considering two additional scattering models, namely, \sin^2 and small-slope approximation (SSA) models. This paper also presents a parallel version of the sampling method to shorten execution time.

C. Sand Ripple Model

A stochastic model for high-frequency and narrow-angle SAS imagery collected over a sand ripple field, originally proposed by Lyons *et al.* [2], represents the image as a product between a process governing the speckle in the imagery, $Z(r, x)$, and a process governing the amplitude of a pixel's scattering strength, $a(r, x)$, i.e.,

$$Y(r, x) = Z(r, x)a(r, x) \quad (1)$$

where r and x are the down- and cross-range image dimensions, respectively. In this model, considering only the down-range dimension r , the amplitude of a pixel's scattering strength is approximated by

$$a(r) \simeq \sigma_s(\theta_0) + [\sigma_s(\theta_{\max}) - \sigma_s(\theta_{\min})] \frac{g(r) - \bar{g}}{g_{\max} - g_{\min}} \quad (2)$$

where $\sigma_s(\theta)$ is the scattering cross section at the grazing angle θ , $g(r)$ is the slope of the seafloor at range r , and θ_0 is the average grazing angle. The max and min values are the extremal values of θ and g around the local grazing angle, and \bar{g} is the average slope. The scattering cross section is a common statistical model describing seafloor scattering where acoustic waves are randomly scattered by irregularities on the seafloor. It measures the redistributed acoustic energy caused by the scattering process [28]. Equation (2) is graphically depicted in Fig. 2.

In our work, the speckle noise $Z(r, x)$, which is assumed to follow a K -distribution with a large shape parameter, is approximated using a Rayleigh distribution. Since the Rayleigh distribution has only one scale parameter s , tuning this parameter can only change the noise scale, whereas the shape of the

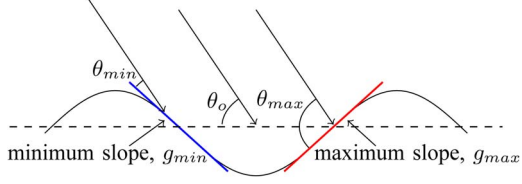


Fig. 2. Graphical depiction of the original sand ripple scattering model from [2].

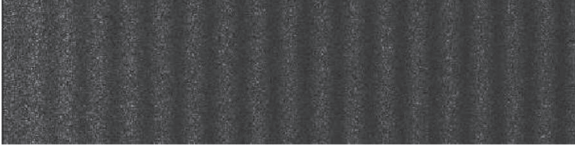


Fig. 3. Synthetic ripple field generated using the model in [2] with a sine-wave bathymetry profile. In this figure, $\sigma_s(\theta)$ was simulated using a normal distribution function centered at $\theta = \pi/2$. The speckle term $Z(x, y)$ for this image was generated using a Rayleigh distributed speckle with a parameter value of $s = 1 \times 10^2$.

probability mass function of the noise remains unchanged. An example of a synthetic ripple field generated using this model is shown in Fig. 3.

D. Overview of the Proposed Method

In this paper, we further develop Lyons' stochastic model by refining the scattering cross-sectional function based on (2) to explicitly incorporate the occlusion from preceding peaks in the sand ripple field. Then, using this expanded model, the parameters governing the bathymetry profile (i.e., the frequency, amplitude, and orientation of the peaks in the sand ripple height field) are estimated from SAS imagery using a hierarchical Bayesian framework in conjunction with a Metropolis-within-Gibbs sampling algorithm.

The expanded sand ripple field model is defined in Section II. Section III describes the proposed hierarchical Bayesian framework and the Metropolis-within-Gibbs sampling algorithm used to estimate the desired parameters from both single passes over an area and using multiple aspects and passes over an area at a variety of ranges. Section IV includes experimental results on simulated and measured SAS imagery. Section V summarizes the research and discusses future work.

II. OCCLUDED SAND RIPPLE MODEL

The proposed method estimates bathymetry information (i.e., sand ripple field height) by leveraging occlusions in the imagery caused by preceding peaks in the sand ripple field. To accomplish this, the model in (2) is expanded to explicitly include a scattering cross-sectional function that incorporates occlusion of scattering from the ripple trough by the preceding peaks. In this expanded model, a function ψ_s replaces σ_s in (2), i.e.,

$$a^*(r, A_H, f, \beta) \simeq \psi_s(\theta_0, r) + [\psi_s(\theta_{\max}, r) - \psi_s(\theta_{\min}, r)] \cdot \frac{g(r) - \bar{g}}{g_{\max} - g_{\min}} \quad (3)$$

with

$$\psi_s(\theta, r) \triangleq \begin{cases} 0 & \text{if } 2 \cdot A_H - \frac{A_S \cdot g(r)}{r - g(r)} \geq h(r) \\ \sigma_s(\theta) & \text{otherwise} \end{cases} \quad (4)$$

where A_H is the ripple amplitude, f is the ripple frequency, β is the ripple orientation, A_S is the height of the SAS array from the seafloor, and $h(r)$ is the ripple height at range r . Note that an estimate of A_S is measured and provided by the SAS sensor for each downrange location. However, the A_S value is dependent on the seafloor characteristics below the sensor. For example, if the SAS array is located above the sand ripple, then the A_S value will depend on whether the measurement is collected over a peak or trough of the sand ripple field.

Given the multiplicative noise model in the sand ripple model in (1), noise is multiplied to the scattering strength $a^*(r, x)$. Thus, given a response of zero in the occluded regions as shown in (4) and given that the input imagery are normalized during preprocessing, the speckle noise scale level should have no significant impact on the simulated SAS imagery and our proposed estimation method. However, noise due to multipath effects may cause a nonzero response in the occluded regions in real measured imagery. The impact of the noise is dependent on the ability to accurately locate the occluded regions. For imagery with noise that causes a nonzero response in the region of occlusion, a preprocessing step in which the occluded regions are detected and set to zero would allow for application of the proposed method without any change in performance.

A. Ripple Height Field

Sand ripples can be approximated by sinusoidal shapes [2]. Assume that the along-crest orientation is perpendicular to the down-range direction, then the ripple height at (r, x) can be defined as

$$h(r, x) \simeq A_H \sin(2\pi f r + b) + A_H \quad (5)$$

where f and b are the sand ripple frequency and phase values, respectively. In practice, since the along-crest orientation of the sand ripple is rarely parallel to the down-range direction, we also introduce into (5) the ripple orientation β , i.e.,

$$h(r, x) \simeq A_H \sin(2\pi f \cos(\beta)r - 2\pi f \sin(\beta)x + b) + A_H \quad (6)$$

where β is the angle between the ripple along-crest orientation and the down-range axis. For each fixed x , the ripple field height at range r can be simplified to

$$h(r) \simeq A_H \sin(2\pi f \cos(\beta)r + b') + A_H \quad (7)$$

where $b' = -2\pi f \sin(\beta)x + b$. Thus, for each x , the ripple height $h(r)$ is still a sine curve with identical amplitude A_H and frequency $f \cos(\beta)$, but with varying phase b' . The ripple slope field at range r can then be computed as

$$h'(r) = g(r) \simeq 2\pi f \cos(\beta) A_H \cos(2\pi f \cos(\beta)r + b'). \quad (8)$$

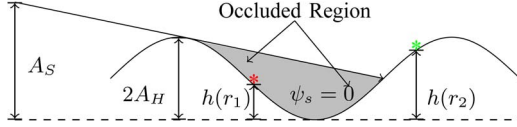
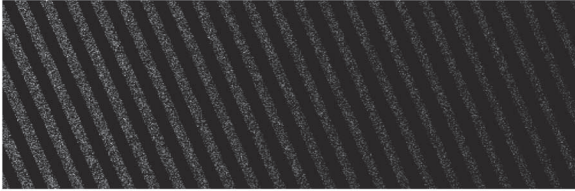


Fig. 4. Expanded model that accounts for shallow grazing angles at long ranges by including the case of occlusion of the ripple trough. The red asterisk is obscured by the preceding peak, whereas the green asterisk is visible by the sonar.



(a)



(b)

Fig. 5. Synthetic ripple field displaying occluded pixels in the trough at long ranges. These shadowed or occluded pixels are typically seen in real imagery. The speckle term $Z(x, y)$ for this image was generated using a Rayleigh distributed speckle with a parameter value of $s = 1 \times 10^2$. (a) $\beta = 0$ (0°). (b) $\beta = \pi/9$ (20°).

In this model, we estimate the ripple height field (i.e., bathymetry) without taking into account any overall seafloor slope. In our future work, we will investigate this factor and incorporate it into (6).

A graphical illustration of the role the additional variables play is depicted in Fig. 4. Synthetic ripple fields with different orientations are generated from this model and shown in Fig. 5. The synthetic ripple field shown in Fig. 5 has larger areas of occlusion at longer ranges as desired. Given this extended model, the relative width of occluded regions provides the needed information to estimate the sand ripple amplitude.

B. Models for Scattering Cross Section

Three models for the scattering cross section σ_s in (4) have been considered in this paper: Gaussian, \sin^2 , and SSA models. The Gaussian and \sin^2 models are simple approximations that are functions only of the slope of the sand ripple field. The SSA model also considers additional parameters such as sound speed in the water, surface roughness, and sediment grain size. Since normalized images are ultimately used in our work, these three models essentially provide us an estimate of the shape of the scattering curve, i.e., the relative scattering level. The absolute scattering level is lost through image normalization and a lack of the appropriate calibration. Fig. 6 shows the scattering cross-sectional curves for the three models that are scaled to the range $[0, 1]$. The purpose of using all three of the Gaussian, \sin^2 , and SSA models in this paper is to show that

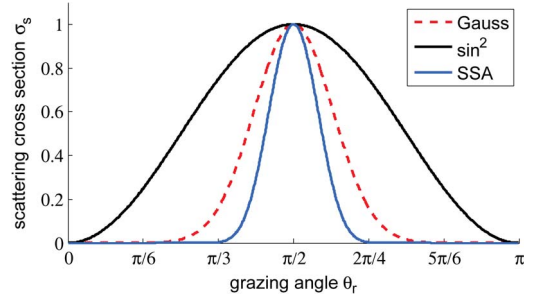


Fig. 6. Normalized scattering cross-sectional curves of Gaussian, \sin^2 , and SSA models. For the Gaussian model, $\sigma_{s,\text{Gauss}}(\theta_r) = \mathcal{N}(\theta_r | \pi/2, (\pi/6)^2)$, and for the \sin^2 model, $\sigma_{s,\sin^2}(\theta_r) = (1/\pi) \sin^2(\theta_r)$. For the SSA model, $a_\rho = 2.0$, and $a_p = 1.1 - 0.1j$. The three curves in the figure are the scattering cross sections when normalized to $[0, 1]$.

our proposed estimation method can be applied to SAS imagery when modeled by a variety of scattering cross-sectional models.

a) Gaussian model: The first scattering cross-sectional model considered is the Gaussian model. In this case, the scattering cross section is approximated as

$$\sigma_{s,\text{Gauss}}(\theta_r) = \mathcal{N}\left(\theta_r \left| \frac{\pi}{2}, \sigma^2 \right.\right). \quad (9)$$

Thus, with this model, the largest response is given when $\theta_r = \pi/2$ since a grazing angle perpendicular to the ripple height field is expected to provide the largest return. In our implementation, the variance of the Gaussian used to model the scattering cross section is set to be $\sigma^2 = (\pi/6)^2$. This variance value was determined based on visual comparisons between data simulated using this model and collected SAS imagery.

b) \sin^2 model: The \sin^2 model is defined as

$$\sigma_{s,\sin^2}(\theta_r) = \mu \sin^2(\theta_r). \quad (10)$$

This model is widely referred to as Lambert's law [28]. For backscattering from a slightly rough surface (e.g., soft sediments), its validity is restricted to oblique incidence angles. On very rough surfaces (e.g., rocky seabed), it is valid over the entire angular domain. The value of μ is often taken to be the empirical Mackenzie coefficient, which is about 0.002 (-27 dB) [29]. If there is no penetration or other losses at the bottom, μ will be -5 dB [30]. In our implementation, since the simulated images are normalized, the choice of μ has no impact on the final simulated image. We simply set μ to be $1/\pi$ (-5 dB).

c) SSA model: As one of the physics-based models for the rough surface scattering problem, the SSA model [28] considers the physical parameters of the seafloor. It takes into account the acoustic frequency and certain roughness-related parameters such as sediment grain size and sediment-water density ratio. The roughness scattering cross section in the SSA model is

$$\sigma_{s,\text{SSA}}(\theta_r) = \frac{k_w^4 |A_{ww}|^2}{2\pi \Delta K^2 \Delta k_z^2} I_k \quad (11)$$

where k_w is the wavenumber in water, ΔK is the magnitude of the horizontal component of the difference of the scattered and incident wave vectors, and Δk_z is the magnitude of the vertical component of this difference. The Kirchhoff integral I_k

given a high-frequency SSA approximation to the seafloor with isotropic roughness statistics is approximated by

$$I_k = \frac{\cot^2(\theta_r)}{R_s^2} e^{-\frac{\cot^2(\theta_r)}{2R_s^2}} \quad (12)$$

where R_s is called the root-mean-square slope. The A_{ww} term is affected by the aforementioned roughness-related parameters and also depends on the choice of wave theory used as discussed in [28, pp. 332–376] and [31]. For a fluid model, a convenient expression for A_{ww} is defined as

$$A_{ww} = \frac{1}{2} [1 + V(\theta_r)]^2 G \quad (13)$$

with

$$G = \left(1 - \frac{1}{a_p}\right) [\cos^2(\theta_r) - B] - 1 + \frac{1}{a_p^2 \cdot a_p} \quad (14)$$

where a_p is the sediment–water density ratio, a_p is the complex ratio of sediment compressional wave speed to water sound speed, and $V(\theta_r)$ is the flat-interface reflection coefficient at θ_r . Values of these parameters depend on the grain size. Refer to [28, pp. 340–341] for more details on the terms B and V .

III. HIERARCHICAL BAYESIAN FRAMEWORK AND METROPOLIS-WITHIN-GIBBS SAMPLER

The proposed method estimates the sand ripple bathymetry by sampling the ripple frequency, amplitude, and orientation (f, A_H, β) using a Metropolis-within-Gibbs sampling algorithm [32], a Markov chain Monte Carlo (MCMC) method that samples from a probability distribution using a Markov chain with the desired distribution as its stationary distribution [33], [34]. The sample set (f, A_H, β) that minimizes the difference between the true image and the corresponding simulated image based on the extended model in (4) is selected as the final estimate. The Metropolis-within-Gibbs sampler allows for generating samples from a multivariate distribution. This approach provides the advantage of being able to estimate a full distribution of possible parameter values given a complex data likelihood and prior distribution while maintaining the convergence guarantees of an MCMC sampling approach. The Metropolis-within-Gibbs sampler was implemented to estimate frequency, amplitude, and orientation characteristics given the following hierarchical Bayesian framework.

A. Hierarchical Bayesian Framework

The data likelihood used in the proposed framework places a Gaussian distribution around an input SAS pixel value given its estimate with the expanded model of the amplitude of the pixel's scattering strength, i.e.,

$$x_{i,r}|A_H, f, \beta \sim \mathcal{N}(x_{i,r}|a^*(r, A_H, f, \beta), \sigma_x^2) \quad (15)$$

where $x_{i,r}$ is the i th pixel in the image at range r . In our work, the pixel values are assumed to be in the range $[0, 1]$. After computing a^* , we normalized it to the range $[0, 1]$. σ_x is set to be 1 so that the majority of the pixel values are still in the range

$[0, 1]$. Then, the likelihood over a set of SAS image pixels, assuming independence, can be defined as

$$\mathbf{X}|A_H, f, \beta \sim \prod_{i=1}^N \mathcal{N}(x_{i,r}|a^*(r, A_H, f, \beta), \sigma_x^2) \quad (16)$$

where N is the total number of pixels in the SAS image under consideration, and \mathbf{X} is the set of these image pixels. By determining the A_H , f , and β values that maximize the likelihood function in (16), the mean squared error between the estimate given the model in (3) and the input data, i.e., \mathbf{X} , is minimized.

In order to constrain the sand ripple characteristics to physically possible values and incorporate any prior information, truncated prior distributions are placed on the A_H , f , and β values. For the first (or single) pass of the data over an area, the prior distributions are truncated uniform distributions, i.e.,

$$A_H \sim \mathcal{U}(A_H|l_{A_H}, u_{A_H}) \quad (17)$$

$$f \sim \mathcal{U}(f|l_f, u_f) \quad (18)$$

$$\beta \sim \mathcal{U}(\beta|l_\beta, u_\beta). \quad (19)$$

The lower and upper truncation points l_{A_H} , u_{A_H} , l_f , u_f , l_β , and u_β are set to constrain the ripple amplitude, frequency, and orientation to physically possible values. These values may also be assigned given additional oceanographic information such as sediment type, wave/current information, etc. For the subsequent passes, the prior distributions are truncated Gaussian prior distributions, i.e.,

$$A_H \sim \mathcal{N}_t(A_H|\mu_{A_H}, \sigma_{A_H}, l_{A_H}, u_{A_H}) \quad (20)$$

$$f \sim \mathcal{N}_t(f|\mu_f, \sigma_f, l_f, u_f) \quad (21)$$

$$\beta \sim \mathcal{N}_t(\beta|\mu_\beta, \sigma_\beta, l_\beta, u_\beta) \quad (22)$$

with

$$\mathcal{N}_t(x|\mu, \sigma, l, u) = \begin{cases} C \mathcal{N}(x|\mu, \sigma), & \text{if } l \leq x \leq u \\ 0, & \text{otherwise} \end{cases} \quad (23)$$

$$C = \frac{1}{\Phi\left(\frac{u-\mu}{\sigma}\right) - \Phi\left(\frac{l-\mu}{\sigma}\right)} \quad (24)$$

where C is the standard normalization for the truncated Gaussian distribution, and $\Phi(\cdot)$ is the cumulative distribution function of the standard normal distribution. The prior parameter values $(\mu_{A_H}, \sigma_{A_H}, \mu_f, \sigma_f, \mu_\beta, \sigma_\beta)$ are set based on estimates given by previous passes over the sand ripple field under consideration.

B. Sampling Method

1) *Metropolis-Within-Gibbs Sampler*: This approach iteratively samples f , A_H , and β using a Metropolis-within-Gibbs algorithm [32]. The sampling algorithm for estimating the values given a single pass of the data is summarized in the pseudocode in Algorithm 1. In the following, each step of the sampling algorithm is described.

Algorithm 1 A Metropolis-within-Gibbs sampler that samples sand ripple frequency, amplitude, and orientation from $\Pi(f, A_H, \beta|\mathbf{X})$. The method used for each step is described in the section shown in parentheses.

-
- 1: Set parameter values and initialize $f^{(0)}$, $A_H^{(0)}$ and $\beta^{(0)}$ (Section III-B3)
 - 2: **for** $k \leftarrow 1$ to N **do**
 - 3: Sample the ripple frequency,
 $f^{(k)} \sim \Pi(f|\mathbf{X}, A_H^{(k-1)}, \beta^{(k-1)})$ (Section III-B1a)
 - 4: Sample the ripple amplitude,
 $A_H^{(k)} \sim \Pi(A_H|\mathbf{X}, f^{(k)}, \beta^{(k-1)})$ (Section III-B1b)
 - 5: Sample the ripple orientation,
 $\beta^{(k)} \sim \Pi(\beta|\mathbf{X}, f^{(k)}, A_H^{(k)})$ (Section III-B1c)
 - 6: **end for**
 - 7: **return** $(f^{(0)}, A_H^{(0)}, \beta^{(0)}, f^{(1)}, A_H^{(1)}, \beta^{(1)}, f^{(2)}, A_H^{(2)}, \beta^{(2)}, \dots, f^{(N)}, A_H^{(N)}, \beta^{(N)})$
-

Algorithm 2 A Metropolis–Hastings sampler that generates $f^{(k)} \sim \Pi(f|\mathbf{X}, A_H^{(k-1)}, \beta^{(k-1)})$.

-
- 1: Generate a candidate f^c from $p(f^c|f^{old} = f^{(k-1)})$ [Equation (25)]
 - 2: Generate a random number u from $\mathcal{U}(0, 1)$
 - 3: **if** $u \leq a(f^c, f^{old} = f^{(k-1)})$ [Equation (26)] **then**
 - 4: Accept f^c , $f^{(k)} = f^c$
 - 5: **else**
 - 6: Reject f^c , $f^{(k)} = f^{(k-1)}$
 - 7: **end if**
-

a) Sample ripple frequency: In a standard Gibbs sampler, the samples $f^{(k)}$, $A_H^{(k)}$, and $\beta^{(k)}$ are drawn directly from the distribution $\Pi(f|\mathbf{X}, A_H^{(k-1)}, \beta^{(k-1)})$, $\Pi(A_H|\mathbf{X}, f^{(k)}, \beta^{(k-1)})$, and $\Pi(\beta|\mathbf{X}, f^{(k)}, A_H^{(k)})$, respectively. As the three distributions for $f^{(k)}$, $A_H^{(k)}$, and $\beta^{(k)}$ cannot be drawn directly, we use a single Metropolis–Hastings step to sample these values. As in a standard Metropolis–Hastings algorithm, a proposal distribution is used to generate sample candidates. Then, a candidate can be accepted as the next sample or rejected according to its acceptance ratio. The Metropolis–Hastings step is summarized in Algorithm 2. In the current implementation, the proposal distribution used to generate a frequency candidate f^c for the sample $f^{(k)}$ is a Gaussian mixture centered on the previous frequency sample value $f^{(k-1)}$, i.e.,

$$p(f^c|f^{(k-1)}) = w_{n,f} \mathcal{N}(f^c|f^{(k-1)}, s_{n,f}) + w_{w,f} \mathcal{N}(f^c|f^{(k-1)}, s_{w,f}) \quad (25)$$

where $w_{n,f}$ and $w_{w,f}$ are fixed parameters such that $w_{w,f} + w_{n,f} = 1$ and $w_{n,f}, w_{w,f} \geq 0$. These are used to determine the relative frequency sampling from a Gaussian whose variance is either relatively small (narrow spread: $s_{n,f}$) or large (wide spread: $s_{w,f}$). The variance values $s_{n,f}$ and $s_{w,f}$ are fixed values used to generate the frequency samples. When sampling

from the narrow Gaussian mixture component, a small area in the parameter space surrounding the current frequency sample is explored to refine the current frequency estimate. Sampling from the proposal distribution using the wide Gaussian mixture component allows for larger exploration of the parameter space. Therefore, the $w_{n,f}$, $w_{w,f}$, $s_{n,f}$, and $s_{w,f}$ values will affect the speed of convergence of the proposed method by balancing the local versus global search parameters. Given this proposal distribution, the acceptance ratio for the frequency values used to evaluate f^c will be

$$a = \frac{\Pi(f^c|\mathbf{X}, A_H^{(k-1)}, \beta^{(k-1)})}{p(f^c|f^{(k-1)})} \frac{p(f^{(k-1)}|f^c)}{\Pi(f^{(k-1)}|\mathbf{X}, A_H^{(k-1)}, \beta^{(k-1)})} = \frac{\Pi(f^c|\mathbf{X}, A_H^{(k-1)}, \beta^{(k-1)})}{\Pi(f^{(k-1)}|\mathbf{X}, A_H^{(k-1)}, \beta^{(k-1)})} \quad (26)$$

where

$$\Pi(f|\mathbf{X}, A_H, \beta) \propto \prod_{i=1}^N \mathcal{N}(x_{i,r}|a^*(r, A_H, f, \beta), \sigma_x^2) \cdot \mathcal{N}_t(f|\boldsymbol{\mu}_f, \sigma_f, l_f, u_f) \quad (27)$$

with $N_t(f|\boldsymbol{\mu}_f, \sigma_f, l_f, u_f)$ as the truncated Gaussian prior distribution in (21). The second equality is the result of the proposal distribution being a symmetric distribution. For the first or only pass over an area, $N_t(f|\boldsymbol{\mu}_f, \sigma_f, l_f, u_f)$ will be replaced by the uniform prior distribution in (18).

b) Sample ripple amplitude: The sampling step for the ripple field amplitude parallels the step for sampling the frequency using the latest sampled frequency value. Again, the proposal distribution is a Gaussian mixture centered on the previous A_H value, i.e.,

$$p(A_H^c|A_H^{(k-1)}) = w_{n,A} \mathcal{N}(A_H^c|A_H^{(k-1)}, s_{n,A}) + w_{w,A} \mathcal{N}(A_H^c|A_H^{(k-1)}, s_{w,A}) \quad (28)$$

where $w_{n,A}$ and $w_{w,A}$ are fixed parameters such that $w_{w,A} + w_{n,A} = 1$ and $w_{n,A}, w_{w,A} \geq 0$. Given that the proposal distribution is symmetric, the acceptance ratio used is

$$a = \frac{\Pi(A_H^c|\mathbf{X}, f^{(k)}, \beta^{(k-1)})}{\Pi(A_H^{(k-1)}|\mathbf{X}, f^{(k)}, \beta^{(k-1)})} \quad (29)$$

where

$$\Pi(A_H|\mathbf{X}, f, \beta) \propto \prod_{i=1}^N \mathcal{N}(x_{i,r}|a^*(r, A_H, f, \beta), \sigma_x^2) \cdot \mathcal{N}_t(A_H|\boldsymbol{\mu}_{A_H}, \sigma_{A_H}, l_{A_H}, u_{A_H}). \quad (30)$$

c) Sample ripple orientation: In accordance with the frequency and amplitude sampling, the proposal distribution is

a Gaussian mixture centered on the previous β value, i.e.,

$$p\left(\beta^c|\beta^{(k-1)}\right)=w_{n,\beta}\mathcal{N}\left(\beta^c|\beta^{(k-1)},s_{n,\beta}\right) \\ +w_{w,\beta}\mathcal{N}\left(\beta^c|\beta^{(k-1)},s_{w,\beta}\right) \quad (31)$$

where $w_{n,\beta}$ and $w_{w,\beta}$ are fixed parameters such that $w_{w,\beta} + w_{n,\beta} = 1$ and $w_{n,\beta}, w_{w,\beta} \geq 0$. Given that the proposal distribution is symmetric, the acceptance ratio used is

$$a = \frac{\Pi\left(\beta^c|\mathbf{X}, f^{(k)}, A_H^{(k)}\right)}{\Pi\left(\beta^{(k-1)}|\mathbf{X}, f^{(k)}, A_H^{(k)}\right)} \quad (32)$$

where

$$\Pi(\beta|\mathbf{X}, f, A_H) \propto \prod_{i=1}^N \mathcal{N}(x_{i,r}|a^*(r, A_H, f, \beta), \sigma_x^2) \\ \cdot \mathcal{N}(\beta|\mu_\beta, \sigma_\beta, l_\beta, u_\beta). \quad (33)$$

2) *Parallel Sampling*: The proposed method needs a large number of samples to estimate the parameters of interest. This can be time-consuming when dealing with a large number of images. Therefore, we consider parallelizing the proposed method by allowing separate processors to generate samples of f , A_H , or β , thus shortening the execution time to generate some fixed number of samples. In our implementation, each processor is assigned to generate the same number of samples. The parameter estimates returned by our implementation are those that were generated with the largest posterior value. Since we are only returning the single sample with the largest posterior, several sampling chains may be run in parallel and a single sample selected among the chains. However, this approach does not decrease any “burn-in” period of the sampler. In addition, if the mean, variance, or any other statistic of the samples needs to be estimated, this approach cannot be used. Instead, parallel MCMC based on methods such as regeneration should be utilized [35], [36].

3) *Initialization and Parameter Settings*: The proposed sampling method requires several parameters to be set prior to running the algorithm. For our current implementation and all of the experimental results shown, initialization for the algorithm and parameters are determined using the following methods.

a) *Initialization*: Prior to sampling, the SAS image being analyzed is smoothed and normalized. To preserve the edges that usually define the boundary between nonshadowed and shadowed region in SAS imagery, a 2-D median filter is employed to remove the noise without blurring edges. Smoothing is done by applying a 2-D median filter to the image and is done to minimize the speckle term in (1) (since the pixel scattering strength $a(r)$ is the term of interest). After smoothing, the image is normalized by subtracting the mean image pixel value and dividing by the maximum image pixel value.

Initial values for the frequency are determined by first computing the frequency of each row using 1-D discrete Fourier transform (DFT) and then using the averaged frequency as the initial estimate. The SAS image being considered contains

the input pixels \mathbf{X} . The A_H values are initialized to the root mean square of the pixel intensity values in the SAS image. The initial values of β are estimated using the Hough line transform method [37]. As shown in Fig. 5, the boundaries between shadowed and unshadowed regions can be interpreted as lines, whose angles can be considered as approximations to ripple orientation. From the Hough transform method, we use the average of the detected line angles as the initial value for β .

b) *Parameter settings*: In the current implementation, the phase value b is fixed to zero. When sampling the ripple frequency, amplitude, and orientation, the parameters of their corresponding truncated prior Gaussian distributions need to be set. The upper and lower truncation points are set to constrain the ripple parameters to physically possible values. In our current implementation, these lower and upper truncation points are set to [0.6, 1.5] cycles/m for f , [0, 0.06] m for A_H , and $[-\pi, \pi]$ for β . However, these values can be easily modified given further constraining prior information (such as prior constrained information derived from oceanographic data).

Parameters for the proposal distributions for f , A_H , and β include $w_{n,f}$, $w_{n,A}$, $w_{n,\beta}$, $s_{n,f}$, $s_{n,A}$, $s_{n,\beta}$, $s_{w,f}$, $s_{w,A}$, and $s_{w,\beta}$. In the current implementation, these values are set to 0.7, 0.7, 0.7, 0.01, 0.01, 0.01, 0.1, 0.1, and 0.1, respectively. Given that the proposed method is a Metropolis-within-Gibbs algorithm, it will benefit from the corresponding convergence guarantees. However, the speed of convergence is dependent on these parameter settings. Future work can include investigating methods to optimize these proposal distribution parameters.

When given only an initial single pass of the data, uninformative priors are used for both of these parameters of interest (as opposed to the truncated Gaussian distributions defined in the previous section). These uninformative priors can be approximated by setting the σ_f , σ_{A_H} , and σ_β values to extremely large variance values relative to the truncation points of the prior. However, when previous aspects and passes over an area of interest have been analyzed, the ripple frequency, amplitude, and orientation estimates obtained from the previous passes can be used to set the prior distribution parameter settings. In these cases, μ_f , μ_{A_H} , and μ_β , can be set to the values estimated from previous passes, and σ_f , σ_{A_H} , and σ_β can be set based on the confidence of these previous estimates.

IV. EXPERIMENTAL RESULTS

The proposed sampling method was applied to simulated and real SAS imagery. Results are shown on these data sets and discussed in the following sections.

A. Image Size Analysis

The first set of experiments examines the role the size of an input image plays. An input image should be large enough to provide enough pixels with statistical consistency to extract the desired sand ripple parameters. However, an image must also be small enough to avoid too much spatial variability across the image sand ripple field since, in this work, (A_H, f, β) are assumed to be constant within an image clip. This experiment aims to determine the lower bound on the image size needed to estimate sand ripple parameters.

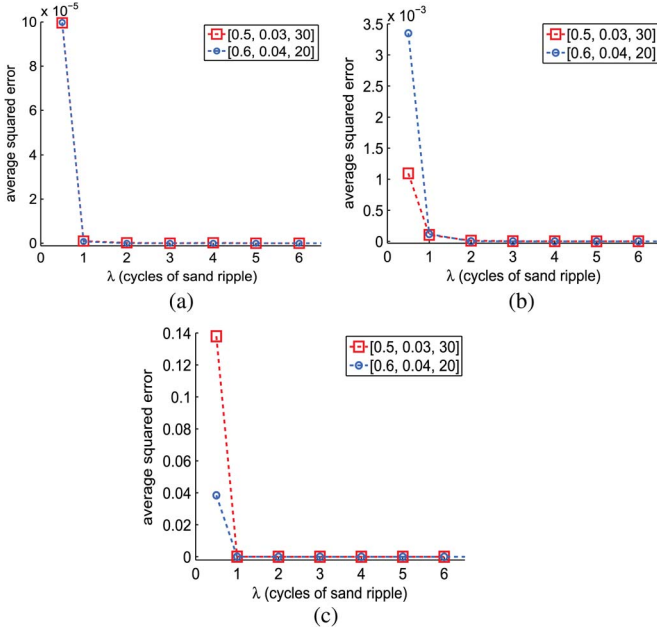


Fig. 7. Average squared error of the estimated (a) ripple amplitude A_H , (b) ripple frequency f , and (c) ripple orientation β under varying number of cycles of sand ripple. The curve with red square markers is for the simulated image with $(f, A_H, \beta) = (0.5 \text{ cycle/m}, 0.03 \text{ m}, \pi/6)$, and the curve with blue circle markers is for the simulated image with $(f, A_H, \beta) = (0.6 \text{ cycle/m}, 0.04 \text{ m}, \pi/9)$.

The proposed method was run ten times on two sets of simulated data generated using the model defined in (1) with the expanded pixel scattering strength model shown in (3) and the Gaussian model as the scattering cross section. The speckle term $Z(x, y)$ in (1) was generated using a Rayleigh distributed speckle with a parameter value of $s = 1 \times 10^2$. One set of the simulated data is generated using the parameter setting $(A_H, f, \beta) = (0.03 \text{ m}, 0.5 \text{ cycle/m}, \pi/6)$ and another one $(A_H, f, \beta) = (0.04 \text{ m}, 0.6 \text{ cycle/m}, \pi/9)$. Each set contains seven square images with a different number of sand ripple cycles $\lambda = \{0.5, 1, 2, 3, 4, 5, 6\}$. The width of each image is determined as $\lfloor \lambda / (f \cdot R) \rfloor$, where R is the sonar range resolution.

Fig. 7(a)–(c) shows the average squared error (over ten runs) of the estimated A_H , f , and β values versus number of sand ripple cycles, respectively. The average squared error stays stable after the “elbow points” in these subfigures. It seems reasonable to conclude that the statistics of the estimates stay consistent when the image covers the area with no less than one ripple. Since the minimum ripple frequency f used in our work is 0.5 cycle/m and the sonar range resolution R is assumed to be 0.025 m , the image width is required to be greater than 160 pixels so that at least two ripples are present in the image; thus, the statistical consistency is guaranteed.

B. Simulated SAS Data—One Pass

In this experiment, three sets of simulated data were generated based on the Gaussian scattering cross-sectional model, the \sin^2 model, and the SSA model. The proposed method was run using sequential and parallel Metropolis-within-Gibbs samplers.

For comparison, a traditional frequency estimation approach where imagery were transformed from the spatial domain into

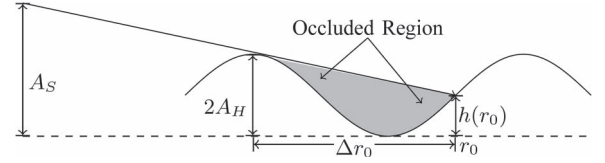


Fig. 8. Geometry-based method of amplitude estimation. $h(r_0)$ is approximated to be zero.

the frequency domain [6], [7] was also employed. A 1-D DFT method is used, which computes the frequency of each image row and takes the average over all row frequencies as the estimate ripple frequency. In our experiments, the sonar range resolution R is assumed to be 0.025 m , and the simulated images are sized to be 400×400 . The DFT length N_{DFT} is 400, and the DFT frequency resolution is $1/(N_{\text{DFT}} \cdot R) = 0.1 \text{ cycle/m}$. Note that in the 1-D DFT approach, only frequency can be estimated. The proposed method is able to estimate ripple frequency, amplitude, and orientation (using the mode of the resulting estimated distributions, i.e., the samples with the largest likelihood value). The proposed method was also compared to a geometry-based method of amplitude estimation (as illustrated in Fig. 8). In the geometry-based method, the shadowed regions are first segmented through thresholding, where a pixel is identified as shadowed if its intensity value is lower than a predefined threshold value. The complete shadowed regions are selected to compute the amplitude (the first and last shadowed regions are excluded). The estimated amplitude for each complete shadowed region is defined as

$$\hat{A}_H \simeq \frac{\Delta r_0}{2r_0} A_S \quad (34)$$

where Δr_0 is the width of the selected shadowed region, and r_0 is the distance from the shadowed region's endpoint to the origin. The average of the estimated amplitudes is used as the final estimated amplitude.

To compare the proposed method with the DFT approach and the geometry-based method and to evaluate the performance of the parallelized sampling method, we have conducted a comprehensive series of experiments, obtaining a large amount of experimental results. Several selected representative experimental results that compare the proposed method to the other methods and examine the performance of parallelized sampling method are shown here. As can be seen in these results, the proposed approach outperforms the traditional DFT approach and the geometry-based method. Furthermore, the parallel sampling approach provides results with a similar error rate but with a significantly shorter running time.

The complete set of experiments is described in the following sections. The geometry-based method shows large variance (instability) in estimated results.

1) *Varying the True f Value:* In this experiment, the f values were varied to be $0.5, 0.6, 0.7$, and 0.8 cycle/m . As the DFT frequency resolution is 0.1 cycle/m , these four ripple frequencies are distinguishable in the 1-D DFT method. The A_H value was set to 0.03 m , the β value is $\pi/6$, and the image clip varied from 0.2 to 10.2 m in range. In all simulated experiments, the height of the SAS array was fixed to 4.0 m . For each f value, the algorithm was run ten times, and a new simulated image was generated for each run.

TABLE I
ONE-PASS SIMULATED DATA—GAUSSIAN MODEL: VARYING A_H , AVERAGE SQUARED ERROR (\pm STANDARD DEVIATION)

True A_H Value		0.02 m	0.03 m	0.04 m	0.05 m
Seq.	A_H	3.9×10^{-9} (3.8×10^{-9})	3.0×10^{-8} (3.8×10^{-8})	2.7×10^{-8} (2.4×10^{-8})	4.3×10^{-8} (6.4×10^{-8})
	f	2.2×10^{-8} (6.0×10^{-8})	5.3×10^{-9} (4.8×10^{-9})	3.0×10^{-9} (3.0×10^{-9})	1.3×10^{-8} (2.6×10^{-8})
	β	6.6×10^{-10} (4.8×10^{-10})	5.8×10^{-10} (9.3×10^{-10})	7.2×10^{-10} (1.2×10^{-9})	3.2×10^{-10} (4.2×10^{-10})
DFT	f	3.7×10^{-2} (1.9×10^{-1})	3.6×10^{-2} (1.9×10^{-1})	3.6×10^{-2} (1.9×10^{-1})	3.6×10^{-2} (1.9×10^{-1})
Geo.	A_H	1.6×10^{-1} (0.0)	1.5×10^{-1} (0.0)	1.5×10^{-1} (2.9×10^{-17})	1.3×10^{-1} (0.0)

The units of the average squared error is m^2 for A_H , $(\text{cycle/m})^2$ for f , and rad^2 for β .

TABLE II
ONE-PASS SIMULATED DATA— \sin^2 MODEL: VARYING β AVERAGE SQUARED ERROR (\pm STANDARD DEVIATION)

True β Value		$\frac{\pi}{6}$	$\frac{\pi}{4}$	$\frac{\pi}{3}$	$\frac{5}{12}\pi$
Seq.	A_H	1.8×10^{-8} (2.3×10^{-8})	1.3×10^{-7} (3.2×10^{-7})	3.6×10^{-8} (5.0×10^{-8})	1.2×10^{-6} (3.5×10^{-6})
	f	8.6×10^{-9} (9.3×10^{-9})	1.5×10^{-8} (2.6×10^{-8})	1.7×10^{-7} (3.0×10^{-7})	3.0×10^{-8} (2.8×10^{-8})
	β	1.8×10^{-9} (4.0×10^{-9})	8.6×10^{-9} (1.5×10^{-8})	1.5×10^{-7} (2.3×10^{-7})	6.0×10^{-8} (5.5×10^{-8})
	Exec.	615.4 seconds	615.0 seconds	606.6 seconds	608.2 seconds
Par.	A_H	2.3×10^{-8} (3.4×10^{-8})	3.5×10^{-7} (2.9×10^{-7})	1.0×10^{-7} (1.3×10^{-7})	2.2×10^{-7} (4.6×10^{-7})
	f	2.9×10^{-8} (4.6×10^{-8})	3.1×10^{-7} (4.6×10^{-7})	1.8×10^{-7} (1.6×10^{-7})	5.7×10^{-7} (8.4×10^{-7})
	β	5.6×10^{-9} (6.3×10^{-9})	3.8×10^{-8} (5.4×10^{-8})	1.9×10^{-7} (7.2×10^{-8})	1.1×10^{-6} (1.4×10^{-6})
	Exec.	153.4 seconds	152.8 seconds	152.4 seconds	152.1 seconds

TABLE III
ONE-PASS SIMULATED DATA—THREE MODELS: VARYING RANGE, AVERAGE SQUARED ERROR (\pm STANDARD DEVIATION) OF A_H

Beginning Range	7.5 m	15.0 m	22.5 m	30.0 m
Gau	3.5×10^{-10} (7.9×10^{-10})	6.3×10^{-9} (3.9×10^{-9})	6.0×10^{-9} (4.4×10^{-9})	8.0×10^{-9} (2.1×10^{-9})
\sin^2	3.2×10^{-10} (9.8×10^{-10})	2.3×10^{-9} (3.0×10^{-9})	4.2×10^{-9} (3.5×10^{-9})	4.6×10^{-9} (3.5×10^{-9})
SSA	2.4×10^{-9} (5.1×10^{-9})	4.0×10^{-9} (3.1×10^{-9})	2.2×10^{-9} (3.3×10^{-9})	3.0×10^{-9} (3.1×10^{-9})

2) *Varying the True A_H Value:* The A_H values were varied to be 0.02, 0.03, 0.04, and 0.05 m, whereas the f value was set to 0.7 cycle/m, the β value is $\pi/6$, and the image clip varied from 0.2 to 10.2 m in range. Again, for each A_H value, the algorithm was run ten times, and a new simulated image was generated for each run. The experimental results using the Gaussian model with a sequential sampling method (as shown in Table I) was selected to show the comparison between the proposed method and the DFT and geometry-based methods. The average squared error of our approach (sequential) is much lower than that of the 1-D DFT method in sand ripple frequency estimation and much lower than that of the geometry-based method in sand ripple amplitude estimation.

3) *Varying the True β Value:* The β values were varied to be $\pi/6$, $\pi/4$, $\pi/3$, and $(5/12)\pi$, whereas the f value was set to 0.7 cycle/m, the A_H value is 0.03 m, and the image clip varied from 0.2 to 10.2 m in range. Again, for each β value, the algorithm was run ten times, and a new simulated image was generated for each run. The experimental results using the \sin^2 model (as shown in Table II) is selected to evaluate the performance of the parallel version of our approach. The parallel sampling approach shortens the execution time by approximately a factor of 4 (the number of processors) and still achieves similar performance to the sequential sampling in terms of average squared error (\pm standard deviation).

4) *Varying the Range of the Simulated SAS Imagery:* The range values were varied to be beginning from 7.5 m in range to 30.0 m in range, whereas the A_H value was set to 0.03 m, and the f value was fixed to 0.7 cycle/m. For each range, the algorithm was run ten times, and a new simulated image was generated for each run. The amplitude estimation results of the Gaussian model, the \sin^2 model, and the SSA model

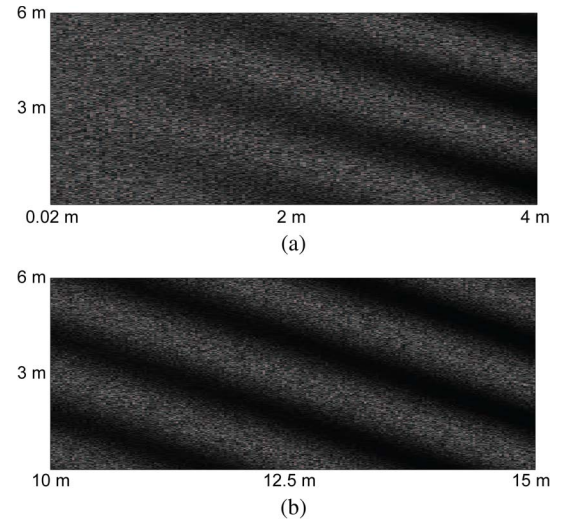


Fig. 9. Image clips with insignificant and significant occluded regions. (a) Insignificant occluded region. (b) Significant occluded region.

using the sequential sampling method are shown in Table III. The proposed method has similar performances on all three models, illustrating that the proposed method can be applied to any appropriate given model.

C. Ripple Orientation Estimation Using the Hough Line Transform Method

As mentioned in Section III-B3a, the Hough line transform method was used for β initialization. For experiments in Section IV-B where obvious occluded regions were present in the simulated imagery, the Hough line transform method could extract the occluded region boundaries precisely, thus

TABLE IV
VARYING β AVERAGE SQUARED ERROR (\pm STANDARD DEVIATION)

True β Value		$\frac{\pi}{6}$	$\frac{\pi}{4}$	$\frac{\pi}{3}$	$\frac{5}{12}\pi$
Seq.	β	8.1×10^{-8} (1.2×10^{-8})	2.2×10^{-8} (5.0×10^{-8})	3.8×10^{-8} (4.3×10^{-8})	5.7×10^{-8} (1.0×10^{-7})
Hough	β	5.4×10^{-4} (0.0)	3.0×10^{-4} (0.0)	1.4×10^{-4} (0.0)	3.4×10^{-5} (0.0)

TABLE V
TWO-PASS SIMULATED DATA: AVERAGE SQUARED ERROR (\pm STANDARD DEVIATION)

True (A_H, f, β)		(0.02 m, 0.8 cycle/m, $\pi/4$)	(0.03 m, 0.8 cycle/m, $\pi/4$)	(0.02 m, 0.9 cycle/m, $\pi/6$)	(0.03 m, 0.9 cycle/m, $\pi/6$)
A_H	Pass 1	2.7×10^{-8} (4.4×10^{-8})	9.5×10^{-9} (1.3×10^{-8})	2.9×10^{-8} (4.6×10^{-8})	3.3×10^{-8} (2.4×10^{-8})
	Pass 2-Uninf.	5.9×10^{-8} (4.8×10^{-8})	1.5×10^{-8} (2.2×10^{-8})	1.6×10^{-8} (2.1×10^{-8})	3.3×10^{-8} (3.1×10^{-8})
	Pass 2-Inf.	1.2×10^{-8} (2.2×10^{-8})	9.4×10^{-9} (1.2×10^{-8})	1.0×10^{-8} (1.1×10^{-8})	1.5×10^{-8} (2.3×10^{-8})
f	Pass 1	1.4×10^{-8} (1.9×10^{-8})	3.2×10^{-8} (5.0×10^{-8})	4.5×10^{-8} (5.9×10^{-8})	1.3×10^{-7} (2.1×10^{-7})
	Pass 2-Uninf.	6.3×10^{-8} (7.1×10^{-8})	9.4×10^{-8} (1.1×10^{-7})	8.4×10^{-8} (1.8×10^{-7})	1.3×10^{-6} (3.1×10^{-6})
	Pass 2-Inf.	1.5×10^{-8} (2.1×10^{-8})	3.6×10^{-8} (6.7×10^{-8})	4.2×10^{-8} (5.9×10^{-8})	1.3×10^{-7} (2.2×10^{-7})
β	Pass 1	5.0×10^{-9} (6.8×10^{-9})	6.3×10^{-9} (8.6×10^{-9})	4.9×10^{-9} (7.1×10^{-9})	2.0×10^{-9} (4.2×10^{-9})
	Pass 2-Uninf.	3.0×10^{-8} (3.0×10^{-8})	2.3×10^{-8} (4.1×10^{-8})	8.7×10^{-8} (2.5×10^{-7})	5.3×10^{-8} (1.7×10^{-7})
	Pass 2-Inf.	4.5×10^{-9} (6.6×10^{-9})	5.9×10^{-9} (7.0×10^{-9})	4.5×10^{-9} (5.9×10^{-9})	1.9×10^{-9} (3.5×10^{-9})

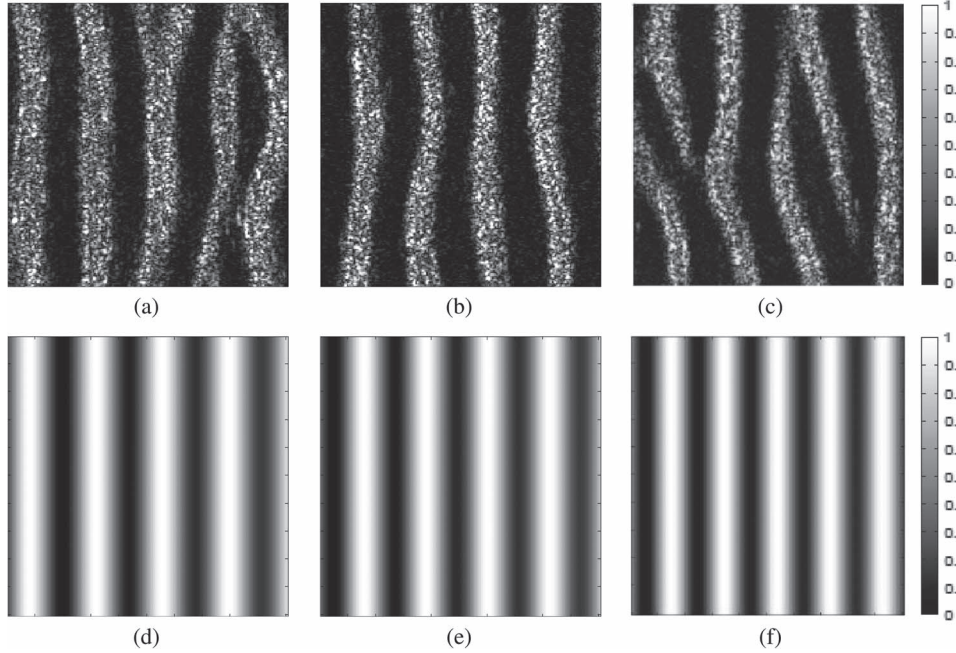


Fig. 10. (a)–(c) Three real image clips. (d)–(f) Corresponding simulated imagery (without speckle) generated using the estimated frequency and amplitude parameters. Estimated results. (a) Estimated $f = 1.05$ cycles/m, $A_H = 0.035$ m. (b) Estimated $f = 0.93$ cycle/m, $A_H = 0.017$ m. (c) Estimated $f = 1.05$ cycles/m, $A_H = 0.016$ m.

providing an accurate initialization. The initial value of β was more accurate than the final estimated β in these cases. However, the performance of the Hough transform approach depends on the occurrence of occluded regions in SAS imagery. In this section, the proposed method was compared with the Hough transform method on images with insignificant occluded regions [as shown in Fig. 9(a)]. The β values were varied to be $\pi/6$, $\pi/4$, $\pi/3$, and $(5/12)\pi$, whereas the f value was set to 0.5 cycle/m, and the A_H value is 0.03 m. The image clip varied from 0.2 to 4.0 m with insignificant occluded regions. For each β value, the algorithm was run ten times, and a new simulated image was generated for each run. Results are shown in Table IV. The Hough line transform method achieved a higher average squared error than the proposed approach when the occluded regions were insignificant.

D. Simulated SAS Data—Multiple Pass

In the first experiment, we have no prior knowledge of the ripple parameters other than knowing physically reasonable values. Thus, for those experiments, we use a uniform prior distribution such that each possible value is treated equally. However, for multiple passes, we can impose prior knowledge from the estimated result of the first pass. By establishing an informative prior distribution for the subsequent passes, the estimated result can be further refined. In this experiment, the informative prior distribution we use is a truncated Gaussian prior distribution centered at the estimated result of the preceding pass [see (20)–(22)]. The σ_f , σ_{A_H} , and σ_β values were set to be 3.00×10^{-6} , based on the squared error computed from simulated data experiments with corresponding parameter settings.

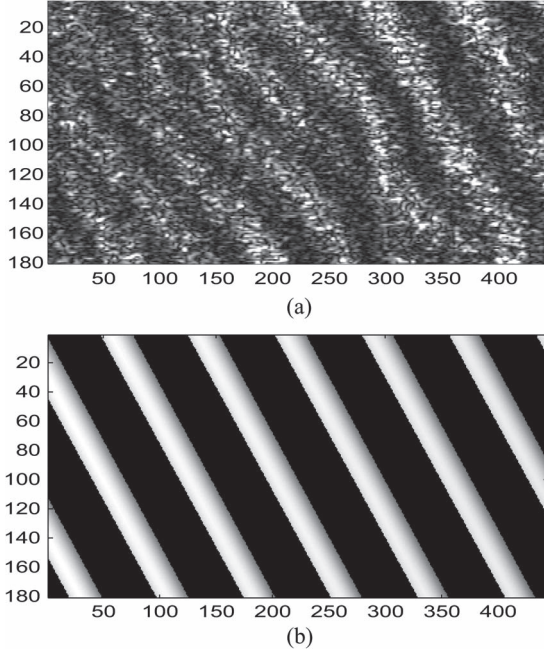


Fig. 11. (a) Real image clip. (b) Corresponding simulated imagery (without speckle) generated using the estimated frequency, amplitude, and orientation parameters. Estimated results: Estimated $f = 1.14$ cycles/m, $A_H = 0.017$ m, and $\beta = 24.9^\circ$.

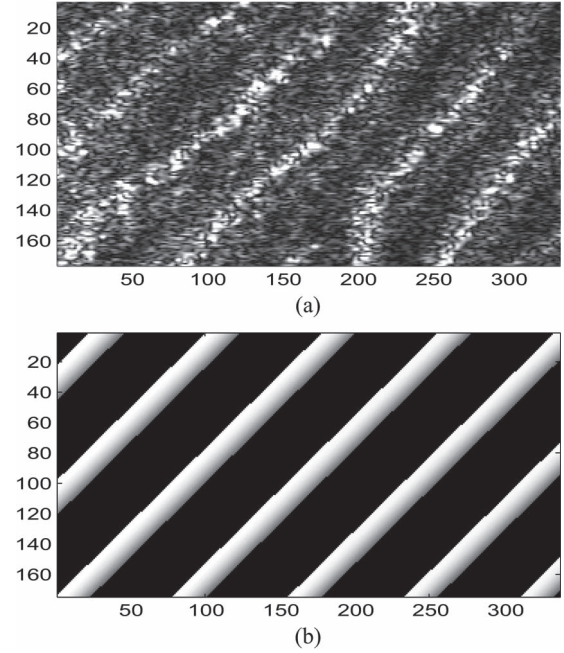


Fig. 12. (a) Another real image clip. (b) Corresponding simulated imagery (without speckle) generated using the estimated frequency, amplitude, and orientation parameters. Estimated results: Estimated $f = 1.22$ cycles/m, $A_H = 0.019$ m, and $\beta = -32.6^\circ$.

Consider the following two-pass experiment. Simulated data for the same area is generated from two different ranges (7.5–27.5 m, 15.0–35.0 m). First, the proposed sampling algorithm with the uniform prior distribution [as described in (17)–(19)] is applied to the first pass of the data with a collection range of 7.5–27.5 m. Then, the second pass (15.0–35.0 m) of the area is analyzed using both the uniform prior distribution (uninformative) and the truncated Gaussian distribution whose parameters are set based on the estimated result of the first pass (informative). In our experiments, we choose four sets of values for (A_H, f, β) , namely, $(0.02, 0.8, \pi/4)$, $(0.03, 0.8, \pi/4)$, $(0.02, 0.9, \pi/6)$, and $(0.03, 0.9, \pi/6)$. For each set, the experiment was run ten times, and the results are shown in Table V. As shown in Table V, the results of the second pass tend to improve overall. This is because more information is available from the second pass due to more regions of occlusion. Imagery that contains more regions of occlusion provides more information when estimating ripple parameters. As the second pass was at larger range values, there were larger regions of occlusion. Furthermore, for two different passes over the same area, two different occlusion regions from the same ripple peaks can be observed. This provides more collaborating information about the height of the ripple field, which is leveraged by the sampling algorithm to improve the overall estimate. Future work will investigate setting prior distribution values based on the relative rates of occlusion in the input imagery.

E. Measured SAS Data

The proposed approach was also applied to real measured SAS imagery. Both single- and multiple-pass experiments were conducted. In the case of real SAS imagery, ground truth

information in terms of true ripple frequency, amplitude, and orientation are unknown. Thus, results are shown with comparison to simulated data generated using the estimated parameter values.

1) *One Pass*: For the one-pass experiments, five real image clips were considered. Three image clips have zero orientation, ranging from 17.1 to 31.7 m. The other two clips have nonzero orientation, ranging from 20.0 to 33.2 m. These experiments were run using the Gaussian scattering cross-sectional model. In Figs. 10–12, we show the image clips used, the resulting estimated parameters, and simulated imagery generated using the resulting ripple frequency and amplitude.

By qualitatively comparing the simulated imagery (without any speckle) to the measured data, we can see that the best results are obtained when the sand ripples do not merge or split. This is due to fixing the phase value b to be zero. Future work will incorporate phase estimates for every pixel in the image (which will result in a considerable increase in the size of the search space). Despite not estimating b , the estimated values for the real imagery appear qualitatively good.

2) *Multiple Passes*: For the multiple-pass experiment, two SAS images collected over the same area from different ranges (21.9–36.6 m and 40.9–50.0 m) were used to estimate the ripple frequency and amplitude. Both of these images are centered over the same sand ripple area with slightly different window sizes. These images were collected several days apart. These figures are shown in Fig. 13. The first pass initially estimated values of $f = 1.464 \pm 0.0092$, $A_H = 0.0595 \pm 0.0004$ (average value over ten runs \pm standard deviation). These values were then used as prior values while incorporating the second pass to refine the estimates. After the second pass, the estimated parameter values for the region were $f = 1.465 \pm 0.0093$,

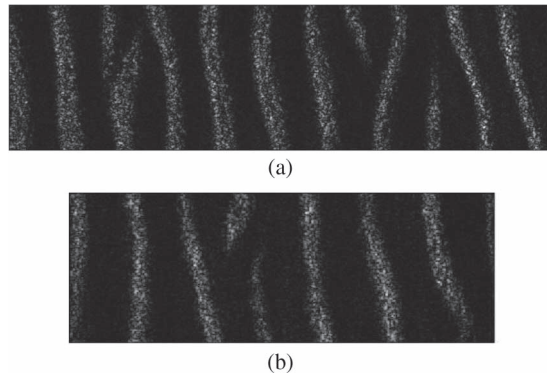


Fig. 13. (a) First and second (b) pass of the rippled sand region collected at 21.9–36.6 m and 40.9–50.0 m in range, respectively.

$A_H = 0.0598 \pm 0.0002$ (average value over ten runs \pm standard deviation).

V. SUMMARY AND FUTURE WORK

This paper extends Lyons' sand ripple model by incorporating occluded/shadowed regions due to the preceding peaks in a ripple field and presents a hierarchical Bayesian framework and MCMC sampling method for sand ripple field frequency, amplitude, and orientation estimation from SAS imagery. Furthermore, the proposed sampling method is parallelized to improve running time. Experimental results show the effectiveness of the extended Lyons' model. When compared with a 1-D DFT method for frequency estimation, a geometry-based method for amplitude estimation, and the Hough transform method for orientation estimation, the proposed sampling method is shown to outperform the others. In comparison, the three sand ripple parameters are simultaneously estimated and have much higher estimation accuracy. The parallel version of the proposed sampling method significantly shortens the execution time by approximately a factor of the number of processors used while preserving the estimation accuracy. Furthermore, multiple-pass experiments show a performance gain by using informative prior information from previous passes over an area.

Future work will include many significant extensions to the proposed approach. The current implementation assumes a flat (nonsloping) seafloor. Future work will include expanding the assumed models and sampling approach to incorporate sloping seafloors. This extension will add additional invariant parameters for estimation (namely, the slope of the seafloor). Furthermore, sand ripple fields do not have a constant phase value, but, instead, ripples merge and split. Therefore, future work will also include estimation of the phase value b for every SAS pixel under consideration. Since the extended sand ripple model is based on Lyons' model, which is only applicable to high-frequency and narrow-angle SAS systems, a more general model suitable to other SAS systems will also be investigated.

ACKNOWLEDGMENT

Any opinions, findings, and conclusions or recommendations expressed in this material are those of the author(s) and do not necessarily reflect the views of the Office of Naval Research.

REFERENCES

- [1] M. P. Hayes and P. T. Gough, "Synthetic aperture sonar: A review of current status," *IEEE J. Ocean. Eng.*, vol. 34, no. 3, pp. 207–224, Jul. 2009.
- [2] A. Lyons, D. Abraham, and S. Johnson, "Modeling the effect of seafloor ripples on synthetic aperture sonar speckle statistics," *IEEE J. Ocean. Eng.*, vol. 35, no. 2, pp. 242–249, Apr. 2010.
- [3] R. E. Hansen, "Introduction to synthetic aperture sonar," in *Sonar Systems*, N. Z. Koley, Ed. Triangle Park, NC, USA: Intech, 2011.
- [4] P. Traykovski, A. E. Hay, J. D. Irish, and J. F. Lynch, "Geometry, migration, and evolution of wave orbital ripples at Leo-15," *J. Geophys. Res., Oceans*, vol. 104, no. C1, pp. 1505–1524, Jan. 1999.
- [5] A. E. Hay and T. Mudge, "Principal bed states during Sandyduck97: Occurrence, spectral anisotropy, and the bed state storm cycle," *J. Geophys. Res., Oceans*, vol. 110, no. C3, Mar. 2005, Art. ID. C03013.
- [6] R. A. Cheel and A. E. Hay, "Cross-ripple patterns and wave directional spectra," *J. Geophys. Res., Oceans*, vol. 113, no. C10, Oct. 2008, Art. ID. C10009.
- [7] I. Maier and A. E. Hay, "Occurrence and orientation of anorbital ripples in near-shore sands," *J. Geophys. Res., Earth Surf.*, vol. 114, no. F4, Dec. 2009, Art. ID. F04022.
- [8] P. L. Wiberg and C. K. Harris, "Ripple geometry in wave-dominated environments," *J. Geophys. Res., Oceans*, vol. 99, no. C1, pp. 775–789, Jan. 1994.
- [9] R. A. Bagnold and G. Taylor, "Motion of waves in shallow water. interaction between waves and sand bottoms," *Proc. R. Soc. Lond. A, Math. Phys. Sci.*, vol. 187, no. 1008, pp. 1–18, Oct. 1946.
- [10] J. B. Southard, J. M. Lambie, D. C. Federico, H. T. Pile, and C. R. Weidman, "Experiments on bed configurations in fine sands under bidirectional purely oscillatory flow, and the origin of hummocky cross-stratification," *J. Sedimentary Res.*, vol. 60, no. 1, pp. 1–17, Jan. 1990.
- [11] M. C. Miller and P. D. Komar, "A field investigation of the relationship between oscillation ripple spacing and the near-bottom water orbital motions," *J. Sedimentary Res.*, vol. 50, no. 1, pp. 183–191, Feb. 1980.
- [12] R. Boyd, D. Forbes, and D. Heffler, "Time-sequence observations of wave-formed sand ripples on an ocean shoreface," *Sedimentology*, vol. 35, no. 3, pp. 449–464, Jan. 1988.
- [13] K. B. Briggs, D. Tang, and K. L. Williams, "Characterization of interface roughness of rippled sand off Fort Walton Beach, Florida," *IEEE J. Ocean. Eng.*, vol. 27, no. 3, pp. 505–514, Jul. 2002.
- [14] K. B. Briggs, "Microtopographical roughness of shallow-water continental shelves," *IEEE J. Ocean. Eng.*, vol. 14, no. 4, pp. 360–367, Oct. 1989.
- [15] R. A. Wheatcroft, "Temporal variation in bed configuration and one-dimensional bottom roughness at the mid-shelf stress site," *Cont. Shelf Res.*, vol. 14, no. 10, pp. 1167–1190, Aug. 1994.
- [16] A. P. Lyons, W. L. Fox, T. Hasiotis, and E. Pouliquen, "Characterization of the two-dimensional roughness of wave-rippled sea floors using digital photogrammetry," *IEEE J. Ocean. Eng.*, vol. 27, no. 3, pp. 515–524, Jul. 2002.
- [17] D. M. Hanes, V. Alymov, and Y. S. Chang, "Wave-formed sand ripples at Duck, North Carolina," *J. Geophys. Res., Oceans*, vol. 106, no. C10, pp. 22 575–22 592, Oct. 2001.
- [18] P. Nielsen, "Dynamics and geometry of wave-generated ripples," *J. Geophys. Res., Oceans*, vol. 86, no. C7, pp. 6467–6472, Jul. 1981.
- [19] A. Skarke and A. C. Trembanis, "Parameterization of bedform morphology and defect density with fingerprint analysis techniques," *Cont. Shelf Res.*, vol. 31, no. 16, pp. 1688–1700, Oct. 2011.
- [20] J. T. Cobb and J. Principe, "Autocorrelation features for synthetic aperture sonar image seabed segmentation," in *Proc. IEEE Int. Conf. SMC*, 2011, pp. 3341–3346.
- [21] J. T. Cobb and J. Principe, "Seabed segmentation in synthetic aperture sonar images," in *Proc. SPIE Defense, Security, Sensing. Int. Soc. Opt. Photon.*, 2011, p. 80170M.
- [22] D. P. Williams and E. Coiras, "On sand ripple detection in synthetic aperture sonar imagery," in *Proc. IEEE ICASSP*, 2010, pp. 1074–1077.
- [23] D. R. Jackson, A. M. Baird, J. J. Crisp, and P. A. Thomson, "High-frequency bottom backscatter measurements in shallow water," *J. Acoust. Soc. Amer.*, vol. 80, pp. 1188–1199, Oct. 1986.
- [24] D. Tang, K. L. Williams, E. Thoros, and K. B. Briggs, "Remote sensing of sand ripples using high-frequency backscatter," in *Proc. MTS/IEEE OCEANS*, 2002, vol. 4, pp. 2081–2085.
- [25] G. Dobeck, "Algorithm fusion for automated sea mine detection and classification," in *Proc. MTS/IEEE OCEANS Conf. Exhib.*, 2001, vol. 1, pp. 130–134.
- [26] G. J. Dobeck and J. T. Cobb, "Fusion of multiple quadratic penalty function support vector machines (QPFSVM) for automated sea mine detection and classification," in *Proc. SPIE*, 2002, pp. 401–411.

- [27] A. Zare and J. T. Cobb, "Sand ripple characterization using an extended synthetic aperture sonar model and MCMC sampling methods," in *Proc. IEEE OCEANS*, 2013, pp. 1–7.
- [28] D. R. Jackson and M. Richardson, *High-Frequency Seafloor Acoustics*. New York, NY, USA: Springer-Verlag, 2007.
- [29] K. Mackenzie, "Bottom reverberation for 530- and 1030-cps sound in deep water," *J. Acoust. Soc. Amer.*, vol. 33, no. 11, pp. 1498–1504, Nov. 1961.
- [30] J. W. Caruthers and J. C. Novarini, "Modeling bistatic bottom scattering strength including a forward scatter lobe," *IEEE J. Ocean. Eng.*, vol. 18, no. 2, pp. 100–107, Apr. 1993.
- [31] D. R. Jackson, "Progress and research issues in high-frequency seafloor scattering," in *Proc. AIP Conf.*, 2004, vol. 728, pp. 125–131.
- [32] S. Chib and E. Greenberg, "Understanding the Metropolis–Hastings algorithm," *Amer. Statist.*, vol. 49, no. 4, pp. 327–335, Nov. 1995.
- [33] W. K. Hastings, "Monte Carlo sampling methods using Markov chains and their applications," *Biometrika*, vol. 57, no. 1, pp. 97–109, Apr. 1970.
- [34] A. F. Smith and G. O. Roberts, "Bayesian computation via the Gibbs sampler and related Markov chain Monte Carlo methods," *J. R. Stat. Soc. Ser. B. Methodol.*, vol. 55, no. 1, pp. 3–23, 1993.
- [35] V. Gopal, "Techniques of parallelization in Markov chain Monte Carlo methods," Ph.D. dissertation, Dept. Stat., Univ. Florida, Gainesville, FL, USA, 2011.
- [36] P. Mykland, L. Tierney, and B. Yu, "Regeneration in Markov chain samplers," *J. Amer. Stat. Assoc.*, vol. 90, no. 429, pp. 233–241, Mar. 1995.
- [37] R. O. Duda and P. E. Hart, "Use of the Hough transformation to detect lines and curves in pictures," *Commun. ACM*, vol. 15, no. 1, pp. 11–15, Jan. 1972.



Alina Zare (S'07–M'08–SM'14) received the Ph.D. degree from the University of Florida, Gainesville, FL, USA, in 2008.

She is currently an Assistant Professor with the Department of Electrical and Computer Engineering, University of Missouri, Columbia, MO, USA.

Her research interests include machine learning, computational intelligence, Bayesian methods, sparsity promotion, image analysis, pattern recognition, hyperspectral image analysis, and remote sensing.

Dr. Zare was a recipient of the 2014 National Science Foundation CAREER Award and the 2014 National Geospatial-Intelligence Agency New Investigator Program Award.



J. Tory Cobb (S'99–M'01) received the B.S. degree in electrical engineering from the U.S. Coast Guard Academy, New London, CT, USA, in 1994, the M.S. degree in electrical engineering from Auburn University, Auburn, AL, USA, in 2001, and the Ph.D. degree from the University of Florida, Gainesville, FL, USA, in 2011.

From 1994 to 1999, he was an active duty officer in the Coast Guard. Since 2001, he has been a Research Engineer at the Naval Surface Warfare Center, Panama City, FL. He has served as a Principal Investigator or Co-Principal Investigator for various automatic target recognition and sensor fusion projects funded by the Office of Naval Research.

His research interests include statistical modeling of sonar signals with applications to automatic target recognition, automated environmental characterization of seabeds in side-look sonar images, and sonar image segmentation algorithm development.

Dr. Cobb is an Associate Editor of the IEEE JOURNAL OF OCEANIC ENGINEERING.



Chao Chen (S'13) received the B.S. and M.S. degree in control theory from Xidian University, Xi'an, China, in 2007 and 2010, respectively. She is currently working toward the Ph.D. degree in the Department of Electrical and Computer Engineering, University of Missouri, Columbia, MO, USA.

Her research interests include sparse coding, Bayesian inference, and synthetic aperture sonar imagery analysis.